



Boosting photoelectrocatalytic hydrogen evolution of Bi@O_v-BiOBr/Cu₃P high-low heterojunction with dual-channel charge transfer

Xibao Li ^{a,b,*}, Tao Han ^a, Yingtang Zhou ^{c, **}, Meng Wang ^b, Zhangliu Tian ^b, Fang Deng ^d, Yidan Luo ^a, Yu Xie ^d, Junlong Huang ^a, Lu Han ^e, Zhi Chen ^a, Zhijun Feng ^a, Wei Chen ^{b,f,***}

^a School of Materials Science and Engineering, Nanchang Hangkong University, Nanchang 330063, China

^b Department of Chemistry, National University of Singapore, 3 Science Drive 3, Singapore 117543, Singapore

^c Zhejiang Key Laboratory of Petrochemical Environmental Pollution Control, National Engineering Research Center for Marine Aquaculture, Marine Science and Technology College, Zhejiang Ocean University, Zhoushan 316004, China

^d National-Local Joint Engineering Research Center of Heavy Metal Pollutants Control and Resource Utilization, Nanchang Hangkong University, Nanchang 330063, China

^e School of Materials and Metallurgy, University of Science and Technology Liaoning, Anshan 114051, China

^f Department of Physics, National University of Singapore, 2 Science Drive 3, Singapore 117542, Singapore



ARTICLE INFO

Keywords:

Photoelectrocatalysis
High-low heterojunction
Hydrogen evolution
Dual-channel
Charge transfer

ABSTRACT

A high-low heterojunction composite, oxygen vacancies BiOBr induced Bi precipitation Bi@O_v-BiOBr/Cu₃P with Bi-O-P chemical bond, was synthesized using a solvothermal method. Compared to single substance, the carrier lifetime and separation rate of Bi@O_v-BiOBr/Cu₃P were significantly improved. According to theoretical calculations and experimental results, Cu₃P can be considered as a hole extractor to accelerate the separation of photogenerated carriers. The successful construction of Bi@O_v-BiOBr/Cu₃P high-low heterojunction with Bi metal can not only activate water molecules and reduce the dissociation energy barrier of water, but also separate and retain the highly reductive electrons. Bi metal and Cu₃P with low valent play a crucial role in dual-channel charge transfer. Bi@O_v-BiOBr/Cu₃P exhibits the highest hydrogen evolution rate up to 723.85 $\mu\text{mol}\cdot\text{cm}^{-2}\cdot\text{h}^{-1}$. It also displays excellent photoelectrocatalytic hydrogen production stability. The boosting hydrogen production activity and stability of Bi@O_v-BiOBr/Cu₃P are attributed to the construction of high-low heterojunctions and the dual-channel charge transfer mechanism.

1. Introduction

The global scarcity of energy resources and the exacerbation of environmental pollution have spurred a collective pursuit of innovative, green, and sustainable energy technologies [1–4]. Photoelectrochemical (PEC) technology driven by solar energy has been regarded as one of the ideal environmental pollution control and clean energy production technologies [5–9]. BiOBr has garnered significant attention within the realm of photocatalysis. It constitutes a prototypical layered material characterized by alternating configurations of bismuth-oxygen layers ($[\text{Bi}_2\text{O}_2]^{2+}$) and halogen layers (X⁻). The atomic layers of BiOBr are linked through van der Waals forces [10–12]. The presence of weak van der Waals forces imparts an open structure to BiOBr, resulting in the

generation of an internal electric field (IEF) between its layers. This IEF serves to facilitate the efficient separation and transfer of photogenerated carriers. BiOBr is extensively employed in diverse applications such as CO₂ reduction, nitrogen fixation, H₂O₂ production, and the degradation of organic pollutants [13–17]. Nevertheless, the substantial drawback in the domain of hydrogen evolution through water splitting stems from the wide band gap (2.6–2.9 eV) inherent in BiOBr. This characteristic results in the rapid recombination of carriers, posing a significant limitation [18,19]. Doping, constructing heterojunctions, and introducing defects are regarded as effective strategies to enhance carrier transport rates [20–25]. Feng et al. [26] documented the synthesis of BiOBr/C Schottky junction composites through chemical vapor deposition (CVD). The hydrogen evolution rate achieved by the BiOBr/C

* Corresponding author at: School of Materials Science and Engineering, Nanchang Hangkong University, Nanchang 330063, China.

** Corresponding author.

*** Corresponding author at: Department of Chemistry, National University of Singapore, 3 Science Drive 3, Singapore 117543, Singapore.

E-mail addresses: lixibao@nchu.edu.cn (X. Li), zhouyingtang@zjou.edu.cn (Y. Zhou), phycw@nus.edu.sg (W. Chen).

Schottky junction in a parallel stacked configuration reached $2850 \mu\text{mol}\cdot\text{g}^{-1}\cdot\text{h}^{-1}$. The notable enhancement in performance was ascribed to the effective formation of the Schottky junction, facilitating rapid carrier separation. Furthermore, the efficacy of oxygen vacancy (O_v) in augmenting photon absorption and diminishing the activation energy of the reaction renders it extensively applied in photoelectrocatalytic water splitting [27,28]. The incorporation of O_v onto BiOBr is deemed a crucial method for enhancing its performance [29]. Tong et al. [30] synthesized ultra-thin BiOBr nanosheets featuring a profusion of oxygen vacancies on the surface, with a significant portion of these vacancies exposed and serving as catalytically active sites. In the photocatalytic reaction involving secondary amines, BiOBr nanosheets with an O_v -rich surface exhibited a twofold increase in the conversion rate, a remarkable 99% selectivity, and maintained high stability. Dong et al. [31] verified that O_v can instigate the creation of intermediate energy levels within the band structure of BiOBr , facilitating the activation of O_2 and resulting in the generation of $\cdot\text{O}_2$ species. The synergistic interplay between bismuth (Bi) elemental presence and oxygen vacancies in O_v - BiOBr demonstrated significantly heightened visible light photocatalytic performance, particularly in the efficient removal of NO .

Ever since Fujiushima and Honda initially achieved PEC hydrogen evolution, numerous semiconductor photoelectrode materials have been devised for this purpose. Examples include metallic oxides (TiO_2 , WO_3 , ZnO , Fe_2O_3 , BiVO_4) [32–36], sulfides (CdS , ZnS) [35,37], nitrides (Ta_3N_5 , GaN) [38,39] and so on. Due to the elevated electronegativity of phosphorus atoms, they possess the capability to absorb electrons from metal atoms. This property leads to a substantial reduction in the overpotential of both the hydrogen evolution reaction (HER) and oxygen evolution reaction (OER). Hence, phosphorus emerges as a favorable substitute for noble metals when utilized as a co-catalyst in the process of photocatalytic hydrogen evolution [40–42]. Lyu et al. [43] fabricated $\text{Ni}_2\text{P}/\text{Ni}_5\text{P}_4$ heterojunctions through a solvothermal method and regulated low-temperature phosphide treatment. Density functional theory (DFT) calculations revealed that the active sites within the interfacial domains exhibit the most favorable adsorption free energy for H^* and the lowest barrier for H_2O dissociation. This phenomenon facilitates electron redistribution and electron structure optimization, consequently enhancing the HER catalytic activity of $\text{Ni}_2\text{P}/\text{Ni}_5\text{P}_4$ nanosheets. Given that Cu_3P functions as a p-type semiconductor, it is commonly regarded as a p-n junction rather than merely a co-catalyst. Yue et al. [44] established a $\text{Cu}_3\text{P}/\text{TiO}_2$ p-n junction to effectively facilitate the separation of photoexcited charges. This approach yielded a notable increase in the H_2 generation rate, reaching 11 times that of pure TiO_2 . Shen et al. [45] reported that the heterojunction effect between the p-type Cu_3P and n-type $\text{g-C}_3\text{N}_4$ can enhance photocatalytic hydrogen evolution more effectively than when Cu_3P is employed solely as a co-catalyst for electron aggregation. Nonetheless, the heterojunction function of Cu_3P in advancing photoelectrocatalytic H_2 generation has been insufficiently explored. In addition, in the traditional heterojunctions, the separation efficiency of electrons and holes is usually not high, and some electrons and holes may recombine, which reduces the efficiency of the photoelectrocatalytic reaction. Using the special energy band structure of heterojunction, the excellent electrical conductivity of metal Bi and the hole extraction characteristics of Cu_3P containing low valent copper to construct high-low junction with dual-channel charge transfer mechanism can not only promote the occurrence of electrochemical reaction, but also improve the reaction rate and reduce the reaction energy loss through the separate transport of electrons and holes during the process of photoelectrocatalytic hydrogen evolution. It can also achieve a unique energy conversion pathway by transferring electrons and holes along the different channels to reduce the probability of two carrier recombination, so as to realize highly efficient photoelectric conversion efficiency and reduce energy loss. Not only that, dual-channel charge transfer can also improve the stability of the material. Due to the separation of the transport channels of electrons and holes, the interaction between the two can be reduced,

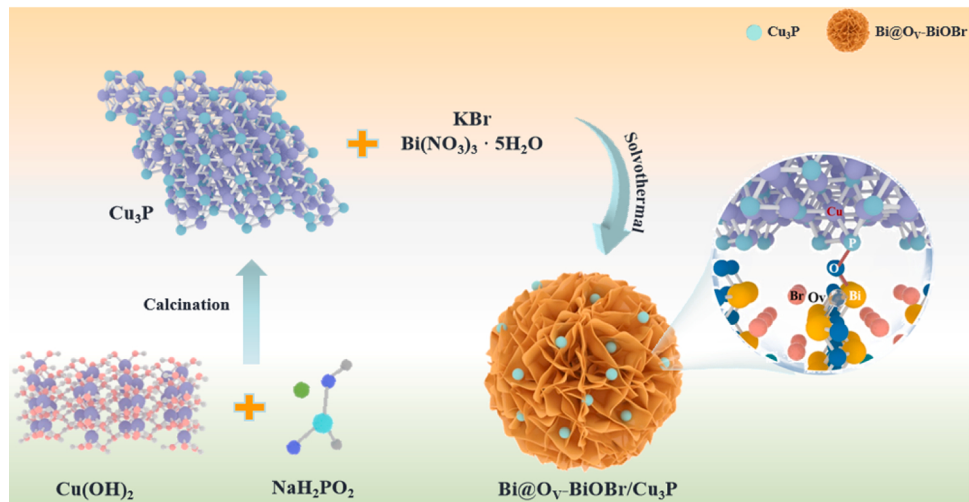
thereby reducing the risk of the material deactivation and prolonging its lifetime. Traditionally, electron and hole transport are often thought of as interrelated processes. In contrast, the dual-channel charge transfer proposed a new way to separate the transport channels of electrons and holes. This novel charge transport mechanism provides a new perspective for us to understand and control the charge transport process, and provides a new idea for designing more efficient and stable functional materials and devices.

In this study, a type-I high-low heterojunction composite with optimal interfacial contact and photoelectrocatalytic hydrogen evolution was constructed by combining $\text{Bi}@\text{O}_\text{v}$ - BiOBr with Cu_3P via high-temperature solvothermal method. Through an in-situ high-temperature solvothermal reaction, Cu_3P is grown on $\text{Bi}@\text{O}_\text{v}$ - BiOBr , resulting in a heterojunction with closely connected interfaces. Cu_3P acts as a hole extractor, efficiently transferring photogenerated holes from $\text{Bi}@\text{O}_\text{v}$ - BiOBr . Simultaneously, in-situ precipitated Bi metal from $\text{Bi}@\text{O}_\text{v}$ - BiOBr serves as a rapid electron transfer channel to the electrode substrate. The synergistic electron-hole dual-channel interface charge transfer effect facilitates swift charge separation and transfer, thereby enhancing the overall photoelectrocatalytic performance. A p-n type $\text{Bi}@\text{O}_\text{v}$ - $\text{BiOBr}/\text{Cu}_3\text{P}$ high-low heterojunction was established, resulting in improved spatial separation of photogenerated charges. This configuration not only retains photogenerated electrons with high reduction potential but also contributes to the outstanding photoelectrocatalytic hydrogen evolution performance. This study delves into the unique dual-channel electron-hole interface charge transfer mechanism of $\text{Bi}@\text{O}_\text{v}$ - $\text{BiOBr}/\text{Cu}_3\text{P}$ photoelectrocatalysts in the context of hydrogen evolution through water splitting. The investigation aims to offer insights into the nuanced understanding of defective high-low heterojunctions applied to photoelectrochemical hydrogen evolution.

2. Results and discussion

2.1. Structure and morphology

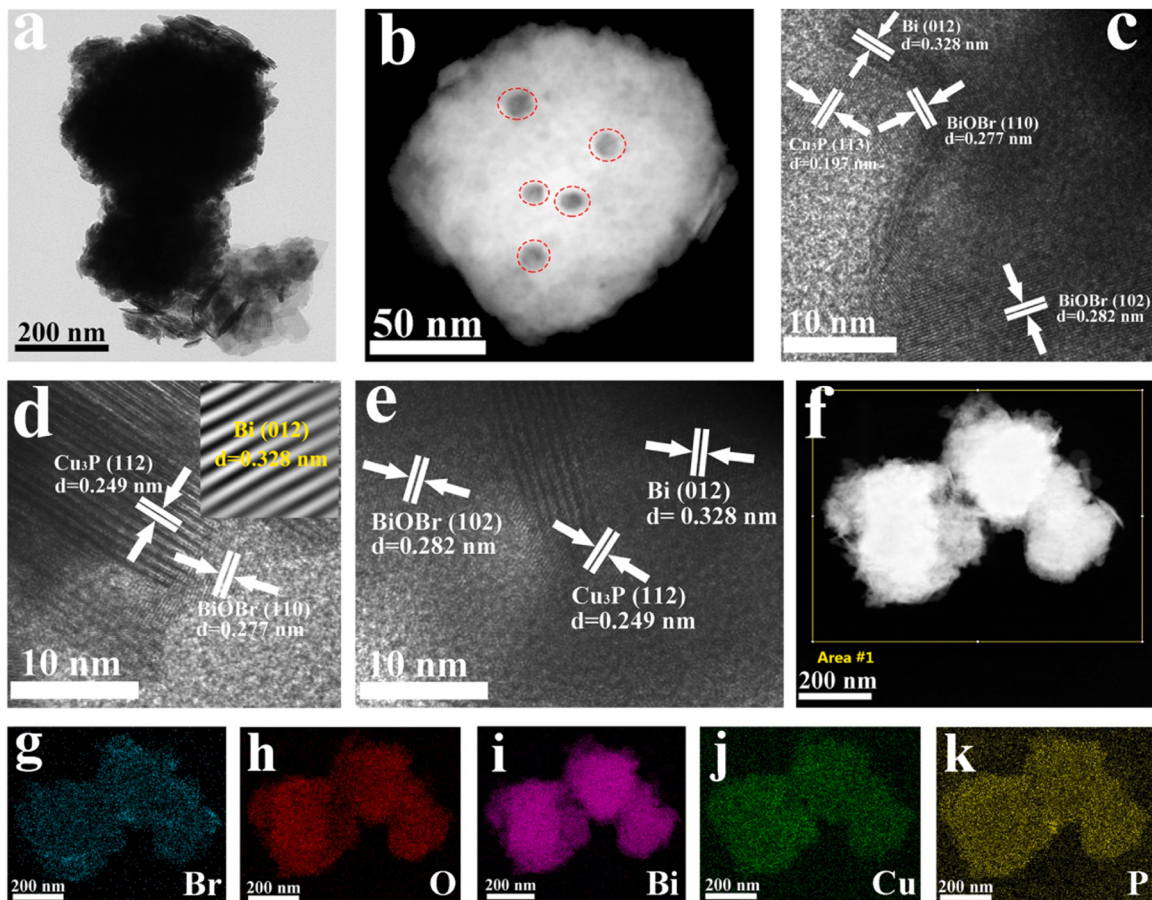
The synthesis of $\text{Bi}@\text{O}_\text{v}$ - $\text{BiOBr}/\text{Cu}_3\text{P}$ involved the addition of KBr and $\text{Bi}(\text{NO}_3)_3\cdot 5 \text{H}_2\text{O}$ to Cu_3P using the solvothermal method, as illustrated in **Scheme 1**. The crystal structures and phases of Cu_3P , BiOBr , $\text{Bi}@\text{O}_\text{v}$ - BiOBr , and $\text{Bi}@\text{O}_\text{v}$ - $\text{BiOBr}/\text{Cu}_3\text{P}$ -X were analyzed via XRD for comprehensive characterization. As shown in **Fig. S1(a)**, the diffraction peaks are attributed to Cu_3P (PDF#71–2261), BiOBr (PDF#09–0393), and Bi (PDF#85–1329). The diffraction peaks of $\text{Bi}@\text{O}_\text{v}$ - BiOBr at 20 are observed at 10.9° , 25.2° , 31.7° , 32.2° , 46.5° , 57.1° , corresponding to the (001), (101), (102), (110), (200) and (212) crystal faces of BiOBr , respectively. Concurrently, the diffraction peaks of Cu_3P at 20 are identified at 36.0° , 39.1° , 41.6° , 45.1° , and 46.2° , corresponding to the (112), (202), (211), (300), and (113) crystal planes. The diffraction peaks at 20 of 27.2° , 37.9° and 39.6° are attributed to the (012), (104) and (110) crystal faces of Bi observed in both $\text{Bi}@\text{O}_\text{v}$ - BiOBr and $\text{Bi}@\text{O}_\text{v}$ - $\text{BiOBr}/\text{Cu}_3\text{P}$, respectively. This phenomenon arises from the high-temperature and high-pressure conditions during the solvothermal process. These conditions lead to the disruption of the Bi-O bond, causing the precipitation of Bi metals from the BiOBr lattice and the formation of O_v . These O_v sites exhibit the capability to trap electrons, facilitating electron aggregation and mitigating the carrier recombination rate of the materials [31]. The characteristic peaks corresponding to the two pure substances are evident in the composites, affirming the presence of O_v - BiOBr and Cu_3P in the composite. Nevertheless, the intensity of the diffraction peak related to Cu_3P in the composite is diminished. This reduction can be attributed to the decrease in Cu_3P content during the solvothermal process and the consequent decline in the fine crystallinity of Cu_3P nanoparticles, leading to the attenuation of its diffraction peak. The characteristic peak of metal Bi in the composite has no obvious change, indicating that the content of precipitated metal Bi hardly changes during the solvothermal process, and the content of metal Bi has nothing to do with the change of Cu_3P content. In **Fig. S1(b)**,

Scheme 1. Preparation process of Bi@Ov-BiOBr/Cu₃P.

the XRD pattern is locally amplified from Fig. S1(a) within the range of 45.5°-48°. A noticeable shift in the diffraction peak of Bi@Ov-BiOBr/Cu₃P, specifically at the crystal plane (113), is observed when compared to Cu₃P. This shift suggests a robust interfacial interaction between Bi@Ov-BiOBr and Cu₃P during the solvothermal synthesis of Bi@Ov-BiOBr/Cu₃P.

The microstructure of Bi@Ov-BiOBr/Cu₃P was meticulously examined through SEM, TEM and HRTEM, with elemental distribution analysis conducted via EDS. As illustrated in Fig. S2(a-c) and Fig. 1

(a-b), the configuration of Bi@Ov-BiOBr/Cu₃P manifests as a flaky-stacked flower cluster, wherein the Cu₃P nanoparticles exhibit an average diameter of approximately 15 nm, showcasing uniform dispersion across the Bi@Ov-BiOBr nanosheets. The HRTEM images in Fig. 1 (c-e) vividly depict discernible lattice fringes within Bi@Ov-BiOBr/Cu₃P. Specifically, the lattice spacing of Bi@Ov-BiOBr measures around 0.282 nm and 0.277 nm, corresponding to its (102) and (110) crystal faces, respectively [30]. Cu₃P exhibits lattice spacing of about 0.197 nm and 0.249 nm for its (113) and (112) crystal faces, respectively [46,47].

Fig. 1. TEM images (a-b) and HRTEM images of Bi@Ov-BiOBr/Cu₃P (c-e); HAADF image of Bi@Ov-BiOBr/Cu₃P (f); elemental mapping of Br, O, Bi, Cu and P (g-k).

The crystal face spacing of about 0.328 nm matches the (012) crystal face of Bi metal [31]. The elemental distributions of Br, O, Bi, Cu, and P (Fig. 1(g–k)) were obtained by mapping the selected region of Fig. 1(f). These five elements distribute evenly in the complex, showing the coexistence of Bi@O_v-BiOBr and Cu₃P in heterojunction. The TEM and HRTEM results further confirmed the Bi@O_v-BiOBr/Cu₃P composite preparation from the micromorphology perspective.

The chemical valence states and bonding configurations of the samples were assessed using X-ray photoelectron spectroscopy (XPS), as illustrated in Fig. 2. Fig. 2(a) presents the comprehensive spectrum of Bi@O_v-BiOBr/Cu₃P, revealing the presence of elements such as Bi, O, Br, Cu, and P. Fig. 2(b–f) further depict the XPS spectra of Bi@O_v-BiOBr/Cu₃P, delineating the chemical valence states of various elements within Bi@O_v-BiOBr and Cu₃P. In Fig. 2(b), distinct peaks at 158.92 and 164.25 eV are identified as Bi 4f_{7/2} and Bi 4f_{5/2}, respectively, indicating the predominant existence of elemental Bi in trivalent states. Additionally, faint peaks at 157.15 and 162.56 eV correspond to Bi⁰, providing evidence for the precipitation of some metallic Bi during the solvothermal process [48]. Fig. 2(c) presents the XPS spectra of O 1s, revealing distinctive peaks. The peak at 529.70 eV is ascribed to the Bi-O bond in Bi@O_v-BiOBr, while the peak at 531.05 eV corresponds to O_v in Bi@O_v-BiOBr. Additionally, the peak at 532.67 eV is attributed to the O-H bond originating from the binding water retained on the surface of the Bi@O_v-BiOBr/Cu₃P-0.2 heterojunction [49]. In Fig. 2(d), the XPS spectrum reveals two distinct peaks with binding energies of 68.06 eV and 69.10 eV, corresponding to Br 3d_{5/2} and Br 3d_{3/2}, respectively, within the Bi-O-Br bond. Fig. 2(e) displays the XPS spectrum of Cu 2p, featuring characteristic peaks at binding energies of 931.78 eV and 951.61 eV, assigned to Cu 2p_{3/2} and Cu 2p_{1/2}, indicative of monovalent copper. Additionally, peaks observed at 940.33 eV and 960.78 eV are attributed to a limited presence of oxidized Cu species, along with satellite peaks [40,50]. Fig. 2(f) illustrates the XPS spectrum of P 2p. The characteristic peak at a binding energy of 131.76 eV is identified as P 2p_{3/4}, typically associated with the oxide of phosphorus. It can be inferred that the peak at 131.76 eV is indicative of the formation of the Bi-O-P bond [51]. The characteristic peak at 128.56 eV is attributed to the Cu-P bond [50]. In conclusion, the successful preparation of the Bi@O_v-BiOBr/Cu₃P heterojunction is evident from the characterization

of XPS characteristic peaks associated with Bi 4f, O 1s, Br 3d, Cu 2p, and P 2p orbitals.

For a clearer characterization of the presence of oxygen vacancies in the materials, Electron paramagnetic resonance (EPR) tests were conducted on the samples (Fig. S3). The results reveal distinct signals at g=2.004 for both Bi@O_v-BiOBr and Bi@O_v-BiOBr/Cu₃P-X. The peak intensity gradually decreases with the increase of Cu₃P content, indicating that the oxygen vacancy decreases with the increase of Cu₃P, which can be attributed to the fact that the introduction of Cu₃P alters the BiOBr lattice structure, and the conditions related to the formation of oxygen vacancy is changed such as additional reaction sites or active centers that promote the adsorption and reaction of oxygen molecules are provided. This observation underscores the effectiveness of altering the Cu₃P content in regulating the concentration of oxygen vacancies in the Bi@O_v-BiOBr/Cu₃P complex.

3. Analysis of photoelectrocatalytic activity

Fig. 3(a) depicts the linear sweep voltammetry (LSV) curves of Cu₃P, Bi@O_v-BiOBr, and Bi@O_v-BiOBr/Cu₃P photoanodes at a scanning rate of 2 mV·s⁻¹ within the voltage range of 1.0–1.5 V vs. RHE. At 1.23 V vs. RHE, Bi@O_v-BiOBr/Cu₃P-0.2 demonstrates the highest photocurrent density at 4.51 mA·cm⁻². This value surpasses that of Cu₃P (0.54 mA·cm⁻²) and Bi@O_v-BiOBr (0.7 mA·cm⁻²) by factors of 8.4 and 6.4, respectively. This enhancement can be attributed to the formation of a heterojunction between Bi@O_v-BiOBr and Cu₃P. The close contact facilitates a dual-channel mechanism for electron and hole transfer, thereby improving the separation and transport efficiency of carriers. Cu₃P serves as a hole extractor, facilitating the transfer of photo-generated holes, while the metallic Bi in Bi@O_v-BiOBr acts as a rapid channel for electron transfer. At 1.50 V vs. RHE, the photocurrent density of Bi@O_v-BiOBr is 2.4 times that of BiOBr. This indicates that the introduction of oxygen vacancies and metallic Bi enhances electron capture, effectively promoting charge separation. In the presence of oxygen vacancies, they can act as transport channels for electrons, thus affecting electrical conductivity of the material. However, an excess of Cu₃P may become an electron recombination center, reducing the photogenerated carrier transfer rate, while insufficient Cu₃P content

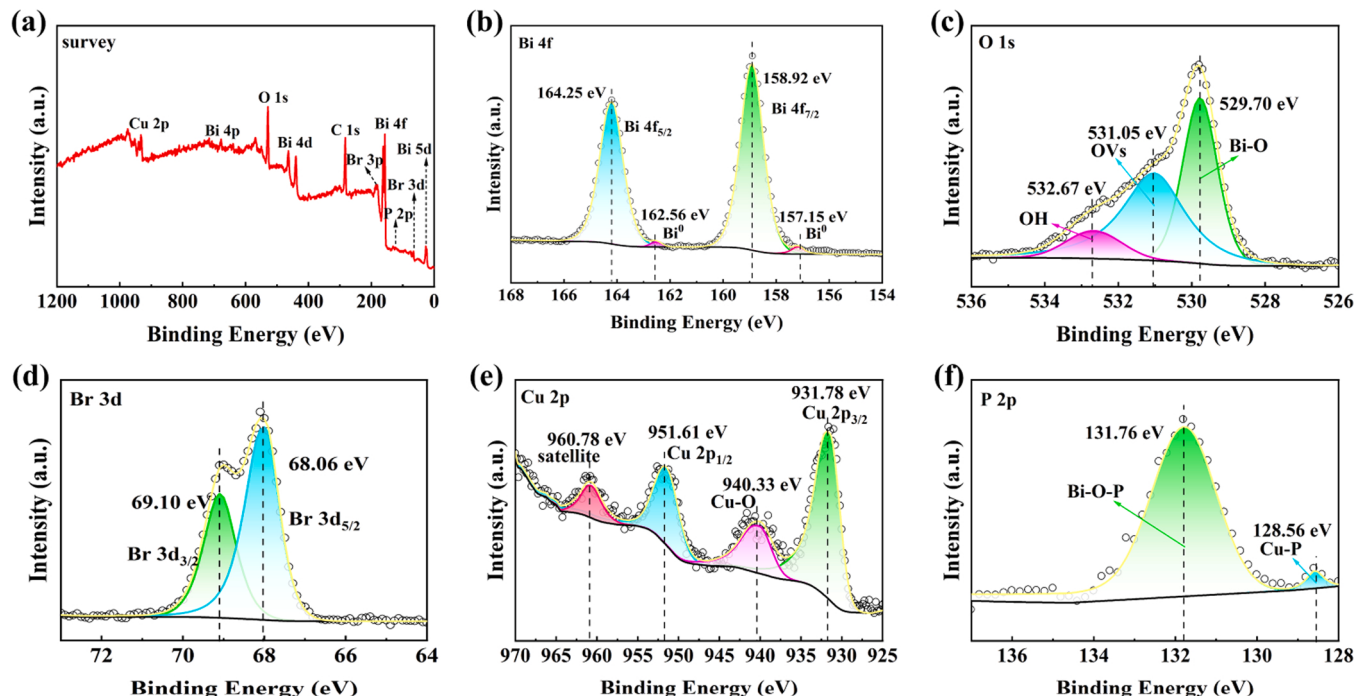


Fig. 2. XPS spectrum (a), Bi 4f (b), O 1s (c), Br 3d (d), Cu 2p (e) and P 2p (f) of Bi@O_v-BiOBr/Cu₃P.

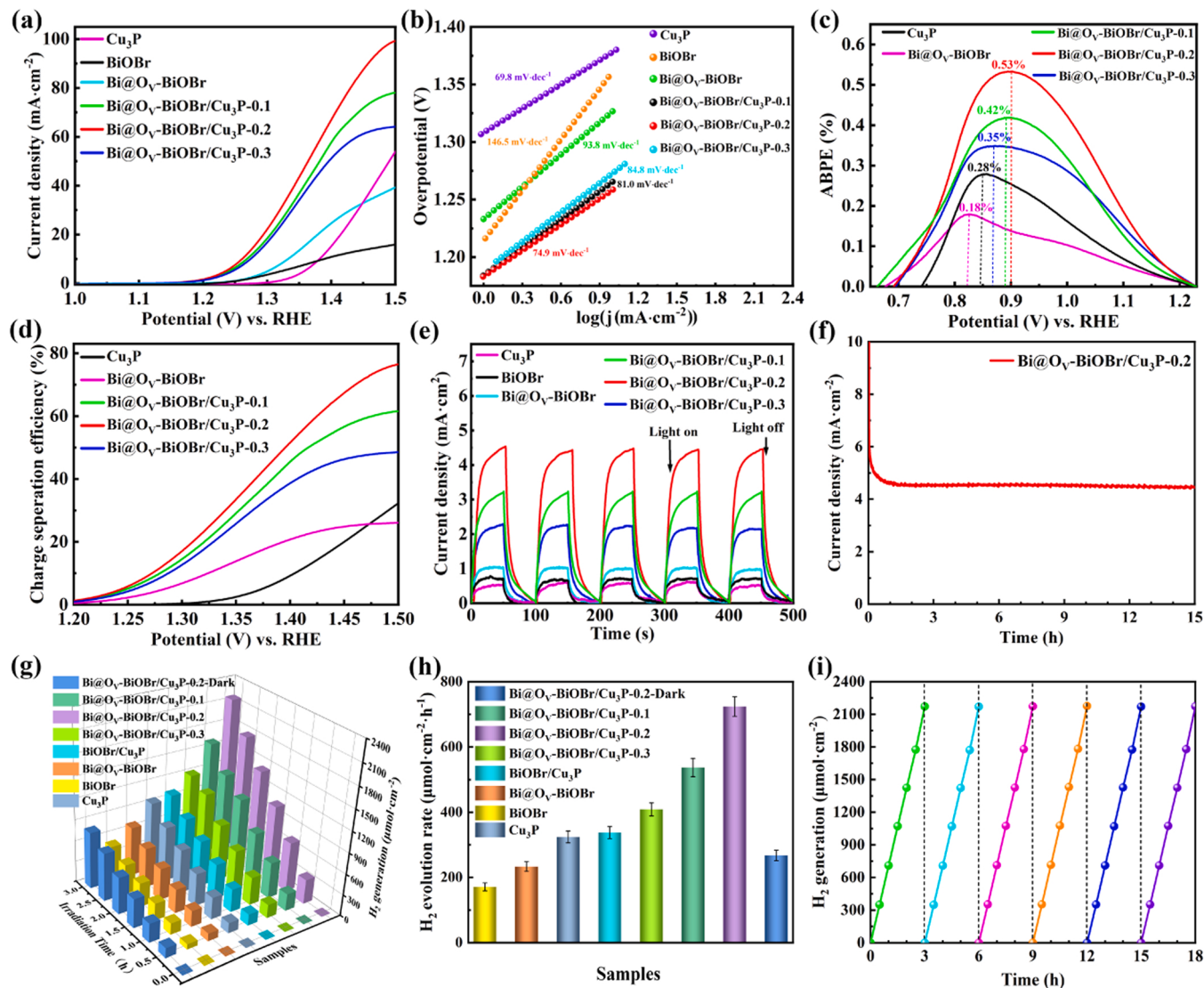


Fig. 3. Linear scanning voltammetric curves (a) and corresponding Tafel curves (b). ABPE plots (c), charge separation efficiency (d) and transient photocurrent responses (e); stability testing of $\text{Bi}@\text{O}_v\text{-BiOBr/Cu}_3\text{P-0.2}$ at 1.23 V vs. RHE (f). Hydrogen evolution volume (g) and hydrogen evolution rate (h) of the samples, hydrogen evolution cycle test of $\text{Bi}@\text{O}_v\text{-BiOBr/Cu}_3\text{P-0.2}$ (i).

hinders the effective transfer of photogenerated holes [52]. Therefore, the $\text{Bi}@\text{O}_v\text{-BiOBr/Cu}_3\text{P-0.2}$ photoanode demonstrates an optimal photocurrent density of $99.33 \text{ mA} \cdot \text{cm}^{-2}$ at 1.50 V vs. RHE. Furthermore, at a photocurrent density of $10 \text{ mA} \cdot \text{cm}^{-2}$, $\text{Bi}@\text{O}_v\text{-BiOBr/Cu}_3\text{P-0.2}$ exhibits the minimum overpotential. The synergistic effect of O_v and the heterojunction formation results in excellent photoelectrochemical hydrogen evolution performance when an appropriate amount of $\text{Bi}@\text{O}_v\text{-BiOBr}$ is combined with Cu_3P . The Tafel diagram, evaluating photoelectrode kinetics and catalytic efficiency, is presented in Fig. 3(b). The Tafel slopes for BiOBr , $\text{Bi}@\text{O}_v\text{-BiOBr}$ and Cu_3P are 146.5, 93.8 and $69.8 \text{ mV} \cdot \text{dec}^{-1}$, respectively. The low Tafel slope of Cu_3P plays a pivotal role in reducing the Tafel slope of $\text{Bi}@\text{O}_v\text{-BiOBr/Cu}_3\text{P}$. Specifically, $\text{Bi}@\text{O}_v\text{-BiOBr/Cu}_3\text{P-0.2}$ exhibits a Tafel slope of $74.9 \text{ mV} \cdot \text{dec}^{-1}$, lower than that of pure $\text{Bi}@\text{O}_v\text{-BiOBr}$. A lower Tafel slope signifies that the catalytic reaction is more facile, indicating relatively superior photoelectrocatalytic performance for $\text{Bi}@\text{O}_v\text{-BiOBr/Cu}_3\text{P}$.

In Fig. S4(a), the LSV diagrams of $\text{Bi}@\text{O}_v\text{-BiOBr/Cu}_3\text{P-0.2}$ are presented under both light and dark conditions. At a voltage of 1.5 V vs. RHE, the photocurrent density of $\text{Bi}@\text{O}_v\text{-BiOBr/Cu}_3\text{P-0.2}$ is observed to be $99.33 \text{ mA} \cdot \text{cm}^{-2}$ under light, displaying a $23.86 \text{ mA} \cdot \text{cm}^{-2}$ increase compared to the dark state. This finding underscores the enhancement in

catalytic performance facilitated by visible light irradiation. Fig. S4(b) illustrates the influence of Na_2SO_3 on the system's performance. Notably, Na_2SO_3 efficiently captures the generated holes, preventing the loss of photogenerated electrons through recombination with holes. Consequently, the separation efficiency of electron-hole pairs is improved. The photocurrent density, when Na_2SO_3 serves as the hole sacrificial agent, is 3.48 times higher than that observed without the sacrificial agent. This substantial increase in photoelectric performance implies that the hole sacrificial agent significantly enhances carrier separation rates and mobility within the composites.

The efficacy of photoanodes in harnessing solar energy for hydrogen production in a semi-electrolytic cell is quantifiable through the applied bias photon-to-current efficiency (ABPE). As depicted in Fig. 3(c), the $\text{Bi}@\text{O}_v\text{-BiOBr/Cu}_3\text{P-0.2}$ exhibits a maximum ABPE value of 0.53% at 0.9 V vs. RHE. This value is 2.9 times higher than that of $\text{Bi}@\text{O}_v\text{-BiOBr}$ (0.18%) and 1.9 times higher than Cu_3P (0.28%). The observed increase in ABPE corroborates the role of Cu_3P in promoting charge transfer by accepting holes, thereby significantly enhancing the water-splitting efficiency at the photoanode. The impact of O_v formation and heterojunction construction on the water-splitting performance of the composite photoelectrodes can be further elucidated by examining

carrier separation and charge transport, as illustrated in **Fig. 3(d)**. The $\text{Bi}@\text{O}_\text{v}-\text{BiOBr}/\text{Cu}_3\text{P}-\text{X}$ composites consistently demonstrate superior charge separation performance when compared to the individual pure substances. This observation suggests that the $\text{Bi}@\text{O}_\text{v}-\text{BiOBr}/\text{Cu}_3\text{P}$ heterojunction effectively achieves spatial separation of photogenerated carriers. In **Fig. 3(e)**, the transient photocurrent of the material is presented. All materials demonstrate a sensitive photocurrent response and maintain a stable photocurrent density. At 1.23 V vs. RHE, BiOBr and Cu_3P exhibit relatively weak photocurrents, while $\text{Bi}@\text{O}_\text{v}-\text{BiOBr}$ shows a discernible enhancement. Notably, $\text{Bi}@\text{O}_\text{v}-\text{BiOBr}/\text{Cu}_3\text{P}-\text{X}$ displays a robust photocurrent response, with $\text{Bi}@\text{O}_\text{v}-\text{BiOBr}/\text{Cu}_3\text{P}-0.2$ achieving a high photocurrent value of $4.51 \text{ mA}\cdot\text{cm}^{-2}$. The introduction of O_v and the formation of high-low heterojunctions accelerate carrier separation and migration, leading to the significantly enhanced photocurrent observed in the optimal ratio of $\text{Bi}@\text{O}_\text{v}-\text{BiOBr}/\text{Cu}_3\text{P}-0.2$. To assess the photoelectrochemical stability of the photoanode, $\text{Bi}@\text{O}_\text{v}-\text{BiOBr}/\text{Cu}_3\text{P}-0.2$ underwent prolonged irradiation under 1.23 V vs. RHE conditions (**Fig. 3(f)**). The results indicate a negligible drop in photocurrent over the 15-hour test period, affirming the remarkable stability of the $\text{Bi}@\text{O}_\text{v}-\text{BiOBr}/\text{Cu}_3\text{P}-0.2$ photoanode. The essentially constant transient photocurrent in **Fig. 3(f)** after multiple cycles of repetition further underscores the robust photoelectrochemical properties of the prepared sample.

Fig. 3(g) illustrates the hydrogen evolution volume of the samples. BiOBr exhibits low hydrogen evolution activity, with a volume of only $513.4 \text{ }\mu\text{mol}\cdot\text{cm}^{-2}$ over 3 h. In contrast, $\text{Bi}@\text{O}_\text{v}-\text{BiOBr}$ demonstrates improved performance, yielding a hydrogen evolution volume of $700.5 \text{ }\mu\text{mol}\cdot\text{cm}^{-2}$ at 3 hours, representing a 1.4-fold increase over pristine BiOBr . This enhancement is attributed to the effective electron capture and charge transfer facilitated by O_v and Bi metal in $\text{Bi}@\text{O}_\text{v}-\text{BiOBr}$. Oxygen vacancies accompany the precipitation of Bi metal, and samples without oxygen vacancies also lack Bi metal, which is not conducive to catalytic activity. Upon the introduction of Cu_3P , a heterojunction is formed between $\text{Bi}@\text{O}_\text{v}-\text{BiOBr}$ and Cu_3P , resulting in a substantial enhancement in the photoelectrochemical hydrogen evolution activity of the $\text{Bi}@\text{O}_\text{v}-\text{BiOBr}/\text{Cu}_3\text{P}-\text{X}$ electrode. Specifically, $\text{Bi}@\text{O}_\text{v}-\text{BiOBr}/\text{Cu}_3\text{P}-0.2$ achieves the highest hydrogen evolution volume of $2171.55 \text{ }\mu\text{mol}\cdot\text{cm}^{-2}$ within 3 hours. This volume is 3.1 and 2.2 times that of $\text{Bi}@\text{O}_\text{v}-\text{BiOBr}$ and Cu_3P , respectively. This notable improvement is attributed to the optimal amount of Cu_3P in $\text{Bi}@\text{O}_\text{v}-\text{BiOBr}/\text{Cu}_3\text{P}-\text{X}$, facilitating the separation and transport of carriers.

In **Fig. 3(h)**, the hydrogen evolution rate of all samples is presented. Notably, $\text{Bi}@\text{O}_\text{v}-\text{BiOBr}/\text{Cu}_3\text{P}-0.2$ exhibits the highest hydrogen evolution rate at $723.85 \text{ }\mu\text{mol}\cdot\text{cm}^{-2}\cdot\text{h}^{-1}$. This rate is 2.2, 3.1, 2.1, 4.2 and 2.7 times higher than that of Cu_3P , $\text{Bi}@\text{O}_\text{v}-\text{BiOBr}$, $\text{BiOBr}/\text{Cu}_3\text{P}$, pristine BiOBr , and $\text{Bi}@\text{O}_\text{v}-\text{BiOBr}/\text{Cu}_3\text{P}-0.2\text{-Dark}$, respectively. Comparative analysis with materials reported in the literature, as depicted in **Table S1**, reveals that $\text{Bi}@\text{O}_\text{v}-\text{BiOBr}/\text{Cu}_3\text{P}$ showcases superior photoelectrocatalytic hydrogen evolution performance under alkaline and neutral conditions. To further emphasize the stability of the photoelectrode, repeated cycle experiments were conducted to assess the hydrogen evolution of $\text{Bi}@\text{O}_\text{v}-\text{BiOBr}/\text{Cu}_3\text{P}-0.2$. As illustrated in **Fig. 3(i)**, the samples maintain consistently high hydrogen evolution activity and exhibit substantial hydrogen evolution amounts under continuous illumination. This underscores the excellent stability of the photoelectrocatalytic hydrogen evolution of $\text{Bi}@\text{O}_\text{v}-\text{BiOBr}/\text{Cu}_3\text{P}-0.2$.

To elucidate the underlying factors contributing to the enhanced photoelectrochemical performance of $\text{Bi}@\text{O}_\text{v}-\text{BiOBr}/\text{Cu}_3\text{P}-0.2$ photoanodes, electrochemical impedance spectroscopy (EIS) Nyquist diagrams were conducted under open-circuit potential transient (OCPT) conditions. The charge transfer resistance was assessed using analog circuit simulation, with R_s , R_{ct} , CPE , and R_{if} representing solution resistance, interface charge transfer resistance, constant phase element, and closed-loop input resistance, respectively. The semicircle diameter in the electrochemical impedance spectrum reflects the charge transfer resistance (R_{ct}) between the photoanode and the electrolyte, and a smaller semicircle diameter indicates lower charge transfer resistance

[53]. The calculated results of the interfacial charge transfer resistance in **Fig. S5(a)** are presented in **Table S2**. Notably, the R_{ct} of $\text{Bi}@\text{O}_\text{v}-\text{BiOBr}/\text{Cu}_3\text{P}-0.2$ is significantly smaller than that of $\text{Bi}@\text{O}_\text{v}-\text{BiOBr}$ and Cu_3P , suggesting that an appropriate proportion of $\text{Bi}@\text{O}_\text{v}-\text{BiOBr}$ with Cu_3P effectively reduces interfacial charge transfer resistance, thereby accelerating the charge transfer rate. The true catalytic activity of the material was further evaluated by estimating the electrochemical active surface area (ECSA) using electrochemical double-layer capacitance (C_{dl}). The C_{dl} values, calculated from the corresponding CV curves, are presented in **Fig. S5(b)**. Evidently, the C_{dl} value of $\text{Bi}@\text{O}_\text{v}-\text{BiOBr}$ is higher than that of pristine BiOBr , and the C_{dl} value of $\text{Bi}@\text{O}_\text{v}-\text{BiOBr}/\text{Cu}_3\text{P}-0.2$ is 5.6, 3.9, and 1.7 times higher than that of pristine BiOBr , $\text{Bi}@\text{O}_\text{v}-\text{BiOBr}$, and Cu_3P , respectively. This indicates that the presence of O_v and the construction of the heterojunction expose more active sites on the surface of the composites. The EIS and ECSA results collectively demonstrate that $\text{Bi}@\text{O}_\text{v}-\text{BiOBr}/\text{Cu}_3\text{P}-0.2$ exhibits the fastest interfacial charge transfer rate and a large number of catalytic active sites, thus providing further confirmation of its superior photoelectrochemical water-splitting performance.

Semiconductor materials typically undergo a recombination process of photogenerated electron-hole pairs before emitting photons [54]. This recombination releases energy in the form of light, thereby diminishing catalytic activity. In the photoluminescence (PL) spectroscopy depicted in **Fig. S5(c)**, $\text{Bi}@\text{O}_\text{v}-\text{BiOBr}$, Cu_3P , and $\text{Bi}@\text{O}_\text{v}-\text{BiOBr}/\text{Cu}_3\text{P}$ exhibit a wide-band emission peak at 395 nm, attributed to the recombination of photogenerated electron-hole pairs. Notably, the PL strength of the $\text{Bi}@\text{O}_\text{v}-\text{BiOBr}/\text{Cu}_3\text{P}$ composite is significantly weaker compared to the individual $\text{Bi}@\text{O}_\text{v}-\text{BiOBr}$ and Cu_3P . This observation indicates that effective charge transfer at the interface facilitates the rapid and efficient separation of photogenerated electron-hole pairs. Furthermore, time-resolved photoluminescence (TRPL) spectroscopy, as illustrated in **Fig. S5(d)**, validates the transfer and separation efficiency of photogenerated charges. In photocatalysis, a longer carrier lifetime typically signifies higher reaction efficiency [55]. The average lifetime (τ_a) can be calculated using the formula: $\tau_\text{a} = (A_1\tau_1^2 + A_2\tau_2^2) / (A_1\tau_1 + A_2\tau_2)$, where τ_1 and τ_2 represent the emission lifetime, and A_1 and A_2 are the corresponding amplitudes. Evidently, $\text{Bi}@\text{O}_\text{v}-\text{BiOBr}/\text{Cu}_3\text{P}$ exhibits a longer photogenerated carrier lifetime (0.50 ns) compared to $\text{Bi}@\text{O}_\text{v}-\text{BiOBr}$ (0.36 ns) and Cu_3P (0.32 ns). This result further confirms that the dual-channel interface charge transfer mechanism of electrons and holes promotes the rapid separation and transport of charges, consequently prolonging the average fluorescence lifetime of the complex. In summary, the construction of the high-low heterojunction in $\text{Bi}@\text{O}_\text{v}-\text{BiOBr}/\text{Cu}_3\text{P}$ effectively inhibits the recombination of photogenerated electrons and holes, facilitating enhanced charge transfer.

4. Analysis of photoelectrocatalytic mechanism

To delve deeper into the photoelectrocatalytic mechanism of $\text{Bi}@\text{O}_\text{v}-\text{BiOBr}/\text{Cu}_3\text{P}$, we conducted a comprehensive investigation into the photoresponsiveness and band structure of BiOBr and Cu_3P using a photoelectrochemical detection method. The photoresponsive properties of the prepared samples were analyzed through UV-Vis diffuse reflectance spectroscopy (UV-Vis DRS), as illustrated in **Fig. S6**. As depicted in **Fig. S6(a)**, $\text{Bi}@\text{O}_\text{v}-\text{BiOBr}$ exhibits significantly enhanced light absorption in the visible and near-infrared regions compared to BiOBr . This enhancement is attributed to the presence of precipitated Bi metal in $\text{O}_\text{v}-\text{BiOBr}$ [31] as well as the oxygen vacancies that alter the lattice structure and charge distribution, which in turn affects the optical properties of the material. Furthermore, the $\text{Bi}@\text{O}_\text{v}-\text{BiOBr}/\text{Cu}_3\text{P}-\text{X}$ composites demonstrate an augmented photoresponse with an increasing content of the narrow-bandgap semiconductor Cu_3P . This enhancement is ascribed to the strong light trapping ability of the black Cu_3P [45]. The Tauc plot of $\text{O}_\text{v}-\text{BiOBr}$ and Cu_3P is presented in **Fig. S6(b-c)**. The linear portion of the curves is extended to the intersection

with the horizontal axis, allowing the determination of the band-gap widths (E_g) of $\text{O}_\text{V}-\text{BiOBr}$ and Cu_3P , which are found to be 2.50 eV and 1.48 eV, respectively. The Mott-Schottky (M-S) curves of Cu_3P and $\text{O}_\text{V}-\text{BiOBr}$ were obtained and analyzed through corresponding photoelectrochemical experiments, as depicted in Fig. S6(d-e). Different frequencies are discernible in the M-S curves, with the semiconductor type (p or n) determined by the slope of the line. The flat-band potential (E_{FB}) of $\text{O}_\text{V}-\text{BiOBr}$ and Cu_3P is identified as -0.62 eV and 1.12 eV (vs. Ag/AgCl , $\text{pH}=7$), respectively. Subsequently, applying the general hydrogen electrode formula ($E_{\text{NHE}} = E_{\text{Ag}/\text{AgCl}} + 0.197$), the E_{FB} of $\text{O}_\text{V}-\text{BiOBr}$ and Cu_3P is calculated to be approximately -0.42 eV and 1.32 eV (vs. NHE, $\text{pH}=7$). Additionally, the positive slope of the straight portion of the M-S curve for $\text{O}_\text{V}-\text{BiOBr}$ indicates it is an n-type semiconductor, while the negative slope for Cu_3P suggests characteristics of a p-type semiconductor. The conduction band potential (E_{CB}) of the n-type semiconductor and the valence band potential (E_{VB}) of the p-type semiconductor are approximately equal to E_{FB} . Therefore, it can be inferred that the E_{CB} of $\text{O}_\text{V}-\text{BiOBr}$ is -0.42 eV, and the E_{VB} of Cu_3P is 1.32 eV. Finally, by combining the previously determined bandgap values, the energy band structure can be calculated using the formula: $E_g = E_{VB} - E_{CB}$. This calculation yields an E_{VB} of 2.08 eV for $\text{O}_\text{V}-\text{BiOBr}$ and an E_{CB} of -0.16 eV for Cu_3P . Employing this information, the comprehensive band structure of $\text{O}_\text{V}-\text{BiOBr}$ and Cu_3P is visually depicted in Fig. S6(f). Thus, from the energy band structure perspective, the n-type semiconductor $\text{O}_\text{V}-\text{BiOBr}$ and p-type semiconductor Cu_3P can form a type I high-low heterojunction.

To validate the space charge separation properties of the $\text{Bi}@\text{O}_\text{V}-\text{BiOBr}/\text{Cu}_3\text{P}$ complex, Kelvin probe force microscopy (KPFM) studies were conducted under both dark and light conditions. As illustrated in Fig. 4(a), nanoscale Cu_3P particles are uniformly distributed on the surface of $\text{Bi}@\text{O}_\text{V}-\text{BiOBr}$. The surface potential diagram (Fig. 4(b-c)) reveals distinct color variations, emphasizing the heterogeneity of the surface potential. In the line scan surface potential image (Fig. 4(d)), a

noticeable potential drop from point A to point B in the dark state indicates the formation of an internal electric field (IEF) from point A ($\text{Bi}@\text{O}_\text{V}-\text{BiOBr}$) to point B (Cu_3P). Following illumination, while the overall surface experiences an electron loss to the counter electrode, locally, the potential increase at point B surpasses that at point A. This discrepancy suggests that some electrons at point B have been transferred to point A. The increased potential at point B is attributed to the transfer of electrons through metal Bi to compensate for the charge loss at point A. Therefore, the KPFM results affirm the existence of an internal electric field between the heterojunction interface and Bi metal serving as one of the channels for electron transport.

The variation in the binding energy of $\text{Bi}@\text{O}_\text{V}-\text{BiOBr}/\text{Cu}_3\text{P}$ before and after illumination was investigated using in-situ XPS to analyze the transfer of photogenerated electrons and holes at the interface, as depicted in Fig. 5(a-e). Clearly, the characteristic peak of the $\text{Bi}@\text{O}_\text{V}-\text{BiOBr}/\text{Cu}_3\text{P}$ composite photocatalyst undergoes a noticeable shift under light illumination, indicating the transfer of photogenerated electron-hole pairs at the $\text{Bi}@\text{O}_\text{V}-\text{BiOBr}/\text{Cu}_3\text{P}$ interface. In Fig. 5(a), the binding energy of the characteristic peaks corresponding to Bi $4\text{f}_{7/2}$ and $4\text{f}_{5/2}$ decreases from 158.92 and 164.25 eV to 158.68 and 164.07 eV after illumination, implying an increase in their electron density. This phenomenon is also observed in the characteristic peaks of the O 1s and Br 3d profiles (Fig. 5(b-c)). The binding energy of the three characteristic peaks of O 1s decreases from 529.70 , 531.05 , and 532.67 eV to 529.49 , 530.66 , and 532.33 eV. Similarly, the binding energy of the two characteristic peaks in Br 3d decreases from 68.06 and 69.10 eV to 67.90 and 68.95 eV. This analysis indicates an increase in the electron density in $\text{Bi}@\text{O}_\text{V}-\text{BiOBr}$, suggesting that Bi metal can efficiently receive and transfer electrons, serving as a rapid channel for electron transfer. In Fig. 5(d-e), the binding energy of the characteristic peaks corresponding to Cu $2\text{p}_{3/2}$ and $2\text{p}_{1/2}$ increases from 931.78 and 951.61 eV to 932.45 and 952.25 eV, respectively. Additionally, in the spectrum of P 2p , the binding energy of $\text{Bi}-\text{O}-\text{P}$ and $\text{Cu}-\text{P}$ bonds increases from 131.76 and

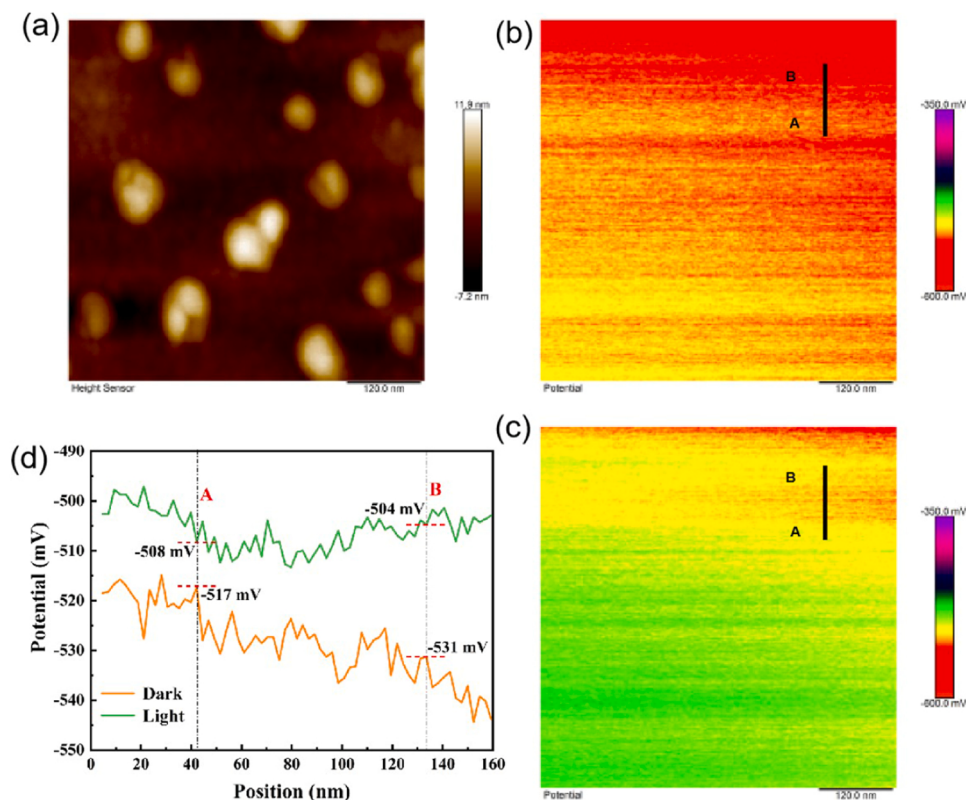


Fig. 4. Atomic force microscopy image of $\text{Bi}@\text{O}_\text{V}-\text{BiOBr}/\text{Cu}_3\text{P}$ (a), surface potential distribution of $\text{Bi}@\text{O}_\text{V}-\text{BiOBr}/\text{Cu}_3\text{P}$ in dark (b) and light (c) conditions, line scanning surface potential from point A to B (d).

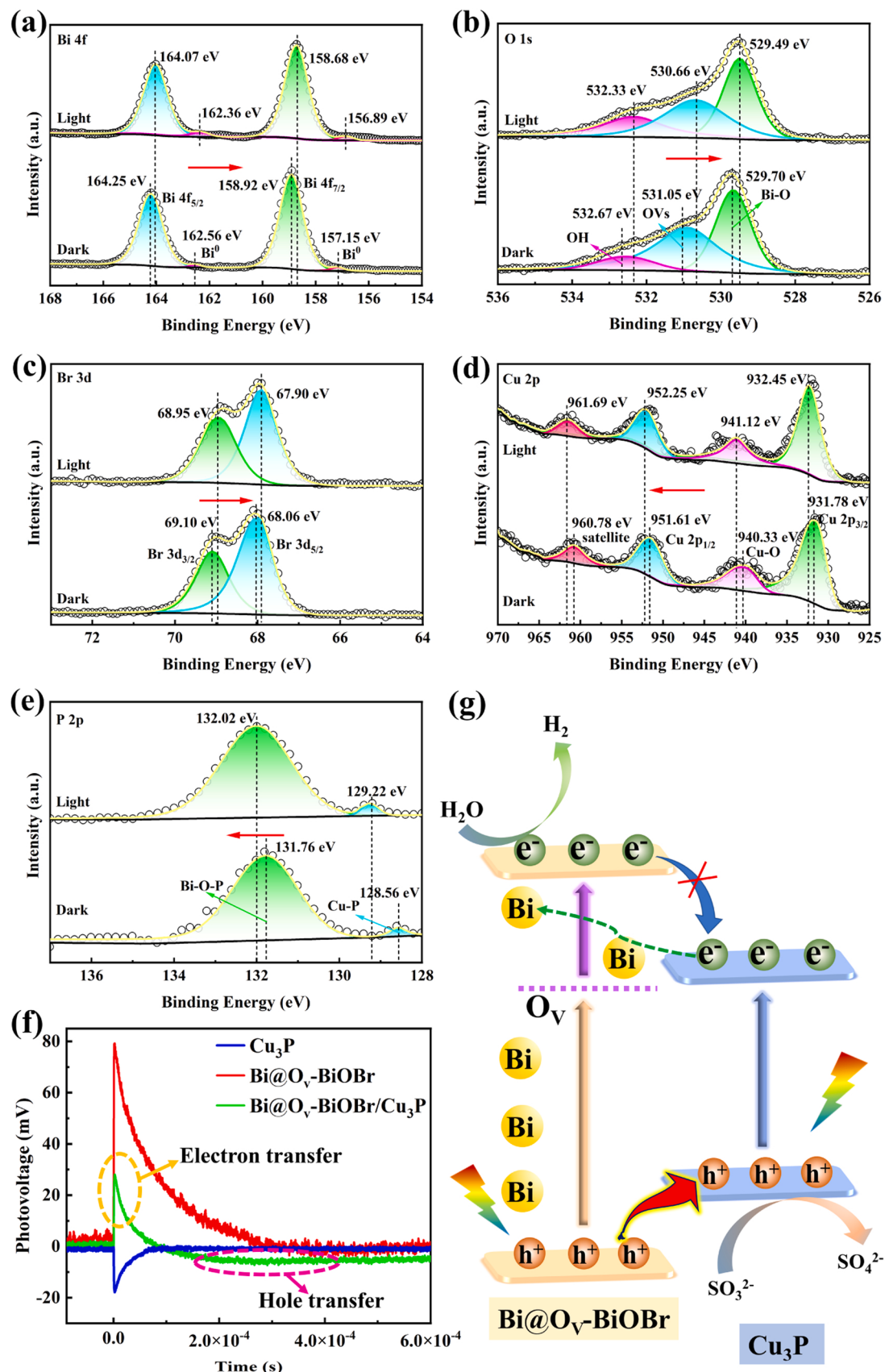


Fig. 5. In-situ XPS spectra of Bi 3d (a), O 1 s (b), Br 4 f (c), Cu 2p (d) and P 2p (e) of Bi@O_v-BiOBr/Cu₃P; TS-SPV responses of Cu₃P, Bi@O_v-BiOBr, and Bi@O_v-BiOBr/Cu₃P (f); schematic diagram of photogenerated carrier transfer at the interface Bi@O_v-BiOBr/Cu₃P (g).

128.56 eV to 132.02 and 129.22 eV, respectively. This shift indicates that Cu_3P can effectively capture the photogenerated holes generated by $\text{Bi}@\text{O}_\text{V}-\text{BiOBr}$ [56].

To further investigate the dynamics of photogenerated carriers in $\text{Bi}@\text{O}_\text{V}-\text{BiOBr}/\text{Cu}_3\text{P}$, transient-state surface photovoltage (TS-SPV) spectra were employed, as illustrated in Fig. 5(f). The positive TS-SPV response of $\text{Bi}@\text{O}_\text{V}-\text{BiOBr}$ indicates that the Bi metal in $\text{Bi}@\text{O}_\text{V}-\text{BiOBr}$ effectively transfers photogenerated electrons. Conversely, the negative TS-SPV signal response of Cu_3P suggests that Cu_3P functions as a hole extractor, transferring photogenerated holes in $\text{Bi}@\text{O}_\text{V}-\text{BiOBr}$. In the

case of the $\text{Bi}@\text{O}_\text{V}-\text{BiOBr}/\text{Cu}_3\text{P}$ complex, the initial positive response signifies the transfer of photogenerated electrons from the Bi metal to the CB of Cu_3P and subsequently to the electrode substrate [57]. Subsequently, the photogenerated holes in $\text{Bi}@\text{O}_\text{V}-\text{BiOBr}$ will transfer to the VB of Cu_3P , facilitating hole transfer at the heterojunction interface. The dual-channel charge transfer mechanism involving both electrons and holes leads to the effective separation of photogenerated carriers, ultimately resulting in a negative response signal in the TS-SPV curve [58]. It should be emphasized that both positive and negative signal responses of TS-SPV can be observed only in the $\text{Bi}@\text{O}_\text{V}-\text{BiOBr}/\text{Cu}_3\text{P}$ composite,

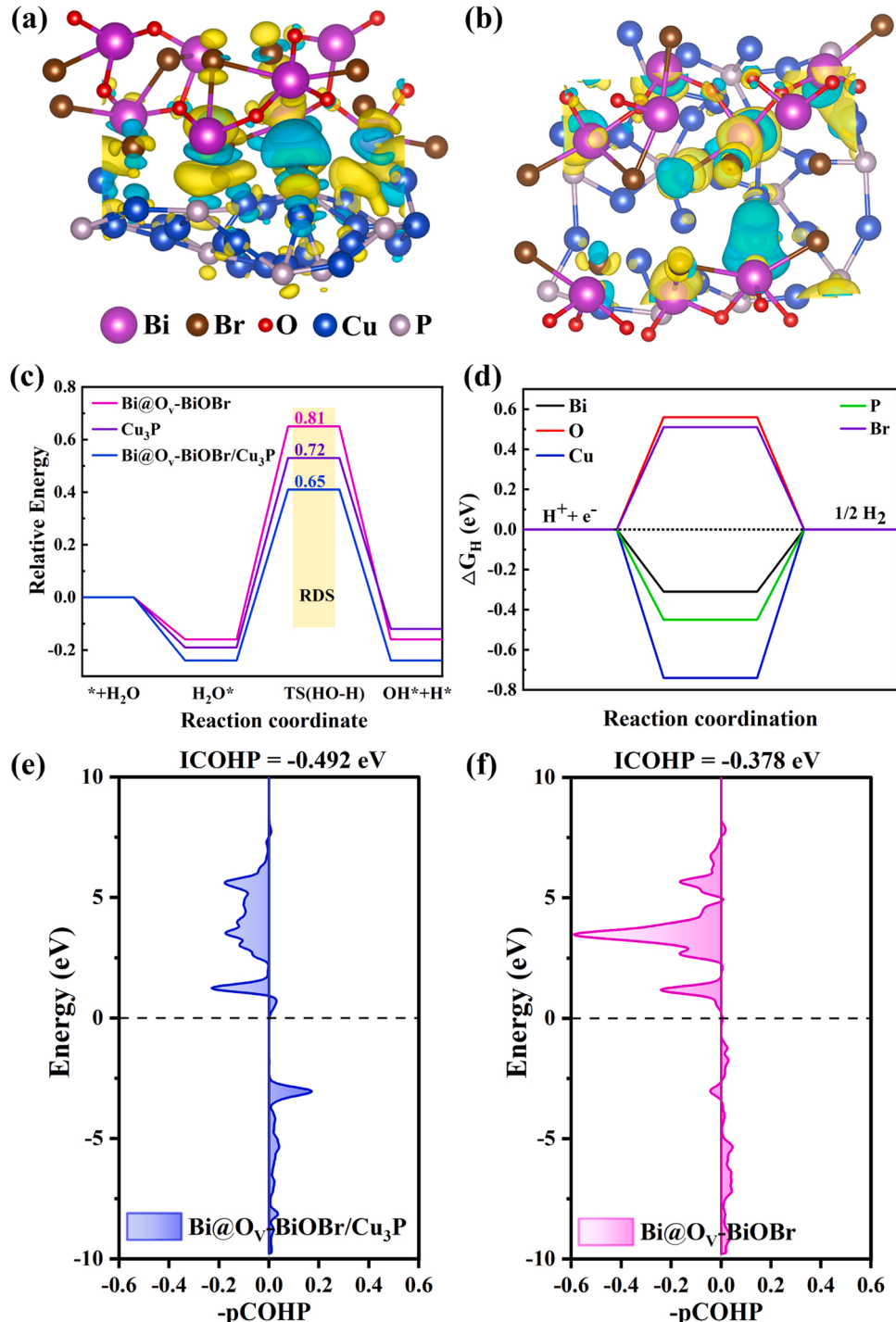


Fig. 6. Charge difference density of $\text{Bi}@\text{O}_\text{V}-\text{BiOBr}/\text{Cu}_3\text{P}$ at different viewing angles (a-b); calculated energy barriers of water dissociation (c); ΔG_H diagram of different sites for $\text{Bi}@\text{O}_\text{V}-\text{BiOBr}/\text{Cu}_3\text{P}$ (d); the ICOHP results of $\text{Bi}@\text{O}_\text{V}-\text{BiOBr}/\text{Cu}_3\text{P}$ (e) and $\text{Bi}@\text{O}_\text{V}-\text{BiOBr}$ (f).

indicating that transfer signals of photogenerated electrons and holes can be clearly detected in the composite. The photogenerated carrier transfer process at the interface of Bi@O_v-BiOBr/Cu₃P is illustrated in Fig. 5(g). Based on the comparative analysis of in-situ XPS and TS-SPV discussed above, it can be inferred that under illumination, the photogenerated holes in Bi@O_v-BiOBr/Cu₃P transfer from Bi@O_v-BiOBr to Cu₃P, while the metal Bi efficiently transfers the photogenerated electrons on the CB of Cu₃P to the external circuit. These provide compelling evidences for the dual-channel transfer mechanism of photogenerated charge at the interface of Bi@O_v-BiOBr/Cu₃P, further confirming the successful coupling of the Bi@O_v-BiOBr/Cu₃P heterojunction.

Determining the work function between semiconductor materials is crucial for studying the direction of interfacial charge transfer. To further explore the charge transfer process at the interface of Bi@O_v-BiOBr and Cu₃P, the work functions of Bi@O_v-BiOBr, Cu₃P, and Bi@O_v-BiOBr/Cu₃P were calculated by density functional theory (DFT) (as shown in Fig. S7(a–c)). The calculated work function of Bi@O_v-BiOBr, Cu₃P and Bi@O_v-BiOBr/Cu₃P was determined to be 3.34, 4.71 and 4.47 eV, respectively. As depicted in Fig. S7(d), Bi@O_v-BiOBr and Cu₃P exhibit distinct work function values. Bi@O_v-BiOBr has a smaller work function compared to Cu₃P. When Bi@O_v-BiOBr and Cu₃P come into contact, electrons spontaneously transfer from Bi@O_v-BiOBr to Cu₃P until the Fermi energy levels of the two reach equilibrium. This electron transfer results in the formation of an electron depletion layer at the interface between Bi@O_v-BiOBr and Cu₃P and an electron accumulation layer at the interface, respectively. Due to the substantial charge accumulation difference on both sides of the interface, an internal electric field (IEF) from Bi@O_v-BiOBr to Cu₃P is formed at their contact interface. The IEF serves as a driving force for the directional movement of photogenerated carriers between different semiconductors. Upon photoexcitation of the catalyst, the IEF effectively facilitates the transfer of photogenerated holes from the VB of Bi@O_v-BiOBr to that of Cu₃P. Simultaneously, due to the repulsive effect of IEF and the energy band bending effect, electrons from the CB of Bi@O_v-BiOBr cannot transfer to Cu₃P. Additionally, owing to the charge transfer between the two semiconductors, the energy band of Bi@O_v-BiOBr bends upward, while the energy band of Cu₃P bends downward, further promoting the movement of photogenerated holes from the VB of Bi@O_v-BiOBr to Cu₃P. The electrons on the CB of Bi@O_v-BiOBr are retained in the high band due to the presence of energy band potential barriers and IEF.

To investigate the charge transfer mechanism in Bi@O_v-BiOBr/Cu₃P, we conducted corresponding DFT calculations. Fig. 6(a–b) illustrates the charge difference density distribution of the Bi@O_v-BiOBr/Cu₃P high-low heterojunction at different angles. The electron cloud density between Bi@O_v-BiOBr and Cu₃P exhibits a clear local distribution, indicating strong bonding interactions between the two substances, forming a high-low heterojunction [59]. Additionally, noteworthy is the accumulation of electrons (depicted in yellow) on the Cu₃P surface, forming an electron accumulation zone, while the Bi@O_v-BiOBr surface is positively charged (depicted in light blue) due to electron loss. Consequently, an IEF is established, pointing from Bi@O_v-BiOBr to Cu₃P at the interface.

Simultaneously, to delve into the internal mechanism governing the photoelectrocatalytic hydrogen evolution performance of Bi@O_v-BiOBr/Cu₃P in an alkaline solution, we conducted DFT calculations to simulate the dissociation of H₂O, as depicted in Fig. 6(c). Notably, the free energy of H₂O dissociation (ΔG_{H-OH^*}) for Bi@O_v-BiOBr and Cu₃P is determined to be 0.81 eV and 0.72 eV, respectively. This suggests a higher activation energy requirement for the dissociation of H₂O on individual Bi@O_v-BiOBr or Cu₃P components. Consequently, the photoelectrocatalytic hydrogen evolution kinetics of Bi@O_v-BiOBr and Cu₃P are characterized by a sluggish pace [60]. Nonetheless, when Bi@O_v-BiOBr and Cu₃P unite to form a heterojunction, the ΔG_{H-OH^*} of Bi@O_v-BiOBr/Cu₃P (0.65 eV) experiences a notable reduction. This reduction suggests that the establishment of the heterojunction plays a crucial role in facilitating the activation of water molecules,

fundamentally enhancing the photoelectrocatalytic hydrogen evolution activity of the materials. To gauge the rate of hydrogen production, we calculated the free energy of the intermediate adsorption state of H^{*}, a parameter denoted as ΔG_H (Fig. 6(d)). A value closer to zero for the difference between the adsorption energy and desorption energy (ΔG_H) of the catalyst for H^{*} signifies higher activity. It is evident that the ΔG_H of the Bi site of Bi@O_v-BiOBr/Cu₃P is closest to zero, indicating that Bi serves as the catalytically active center [61]. In comparison with the Br site ($\Delta G_H = -0.74$ eV), O site ($\Delta G_H = -0.56$ eV), Cu site ($\Delta G_H = -0.45$ eV) and P site ($\Delta G_H = -0.51$ eV) in Bi@O_v-BiOBr/Cu₃P, the ΔG_H of the Bi site is merely -0.31 eV, indicating superior activity. The elevated $|\Delta G_H|$ suggests weak adsorption of H^{*}, directly highlighting that the Br, O, Cu, and P sites are less active in hydrogen evolution reaction, while the Bi site emerges as the active center of Bi@O_v-BiOBr/Cu₃P.

COHP (Crystal Orbital Hamilton Population) analysis is a computational technique used in the field of solid-state chemistry and materials science to understand the bonding interactions between atoms in a crystal. It is an extension of the more general concept of COOP (Crystal Orbital Overlap Population) analysis [62]. As shown in Fig. 6(e–f), the Bi-O atomic interactions between the Bi atom in Bi@O_v-BiOBr/Cu₃P and O in H₂O are stronger compared to those between the Bi atom in Bi@O_v-BiOBr and O in H₂O, as evidenced by the more negative relative ICOHP of Bi@O_v-BiOBr/Cu₃P (-0.492 eV) than that of Bi@O_v-BiOBr (-0.378 eV). This suggests that H₂O molecules favor adsorption on the surface of Bi@O_v-BiOBr/Cu₃P, thereby enhancing the catalyst's kinetic properties and increasing hydrogen production efficiency.

Based on the aforementioned experimental findings, the mechanism underlying the photoelectrocatalytic water splitting for hydrogen evolution in Bi@O_v-BiOBr/Cu₃P was elucidated. As depicted in Fig. 7, the notable difference in work functions between the n-type Bi@O_v-BiOBr and p-type Cu₃P results in the establishment of an internal electric field directed from Bi@O_v-BiOBr to Cu₃P, along with band bending at the contact interface upon the formation of the Bi@O_v-BiOBr/Cu₃P high-low heterojunction. Under visible light irradiation, photogenerated holes on the VB of Bi@O_v-BiOBr migrate to the VB of Cu₃P under the influence of the IEF. Simultaneously, photogenerated electrons on the CB of Bi@O_v-BiOBr remain in its high-energy band due to the repulsion of the IEF and the band bending barrier, enabling efficient spatial separation and transfer of photogenerated carriers. On one hand, the hole extraction effect of Cu₃P and hole sacrificial agent (Na₂SO₃) promptly capture and consume the migrating photogenerated holes, preventing their recombination with the photogenerated electrons. On the other hand, driven by the external bias of PEC and the conductive electron effect of Bi metal, the highly reducing electrons on the CB of Bi@O_v-BiOBr and Cu₃P move to the electrode substrate through the electron transfer channel of metal Bi. Consequently, the dual-channel charge transport functions of Cu₃P's hole extraction and conduction, along with Bi metal's electron conduction, facilitate efficient photogenerated charge separation and transfer, ultimately realizing the high-efficiency photoelectrocatalytic hydrogen production performance of the Bi@O_v-BiOBr/Cu₃P high-low heterojunction.

5. Conclusion

In conclusion, a robust p-n type Bi@O_v-BiOBr/Cu₃P high-low heterojunction composite, exhibiting pronounced photoelectrocatalytic hydrogen evolution activity, was successfully synthesized through a facile solvothermal method. The Bi@O_v-BiOBr/Cu₃P connection is facilitated by the Bi-O-P bond. Under visible light and low applied bias potential, Bi@O_v-BiOBr/Cu₃P demonstrates the highest hydrogen evolution rate of 723.85 $\mu\text{mol}\cdot\text{cm}^{-2}\cdot\text{h}^{-1}$, surpassing BiOBr, Bi@O_v-BiOBr, and Cu₃P by 4.2, 3.1, and 2.2 times, respectively. The findings underscore the efficacy of in-situ Bi metal precipitation and oxygen vacancy introduction in enhancing light absorption and electron separation and transfer. Moreover, the successful integration of Bi@O_v-BiOBr and Cu₃P facilitates a dual-channel electron-hole interface charge transfer

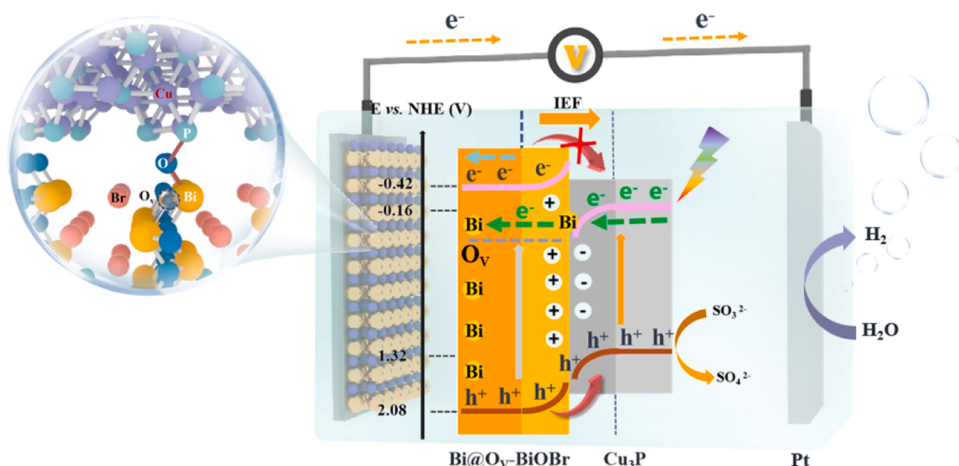


Fig. 7. Schematic diagram of the photoelectrocatalytic HER mechanism of Bi@Ov-BiOBr/Cu₃P.

mechanism in Bi@Ov-BiOBr/Cu₃P. The combined impact of the IEF and energy band bending barriers in the p-n type Bi@Ov-BiOBr/Cu₃P high-low heterojunction ensures the efficient spatial separation of photo-generated carriers. Furthermore, the metallic nature of Bi promotes the transfer of photogenerated electrons from the electrode interior to the external circuit, enhancing electron participation in the hydrogen evolution reaction and ultimately resulting in outstanding photoelectrocatalytic hydrogen evolution performance. This study provides valuable insights and innovative approaches for designing highly efficient photoelectrocatalytic hydrogen production electrode materials endowed with dual-channel charge transport functionality.

6. Methods

Experimental details of the synthesis and characterization of Bi@Ov-BiOBr/Cu₃P composite, including structural and photoelectrochemical tests, and other [supplementary data](#), are provided in the [Supporting Information Appendix](#).

CRediT authorship contribution statement

wei CHEN: Writing – review & editing, Formal analysis. **Tao Han:** Methodology, Data curation. **Yingtang Zhou:** Software, Formal analysis. **Meng Wang:** Visualization, Software. **Juntong Huang:** Supervision. **Lu Han:** Investigation. **Zhi Chen:** Supervision. **Zhijun Feng:** Supervision. **Xibao Li:** Writing – original draft, Investigation. **Zhangliu Tian:** Validation. **Fang Deng:** Methodology. **Yidan Luo:** Formal analysis. **Yu Xie:** Data curation.

Declaration of Competing Interest

The authors declare that they have no known competing financial interests or personal relationships that could have appeared to influence the work reported in this paper.

Data Availability

Data will be made available on request.

Acknowledgements

This work was financially supported by the National Natural Science Foundation of China (22262024, 52272063, 22272070), Jiangxi Province Academic and Technical Leader of Major Disciplines (20232BCJ22008), Key Project of Natural Science Foundation of Jiangxi Province (20232ACB204007), Double Thousand Talent Plan of Jiangxi

Province, Foundation of State Key Laboratory of High-efficiency Utilization of Coal and Green Chemical Engineering (2022-K31) and the Zhejiang Province Key Research and Development Project (2023 C01191).

Appendix A. Supporting information

Supplementary data associated with this article can be found in the online version at [doi:10.1016/j.apcatb.2024.123913](https://doi.org/10.1016/j.apcatb.2024.123913).

References

- [1] Q. Zhou, Y. Guo, Y. Zhu, Photocatalytic sacrificial H₂ evolution dominated by micro pore-confined exciton transfer in hydrogen-bonded organic frameworks, *Nat. Catal.* 6 (2023) 574–584.
- [2] Z. Tian, C. Han, Y. Zhao, W. Dai, X. Lian, Y. Wang, Y. Zheng, Y. Shi, X. Pan, Z. Huang, H. Li, W. Chen, Efficient photocatalytic hydrogen peroxide generation coupled with selective benzylamine oxidation over defective ZrS₃ nanobelts, *Nat. Commun.* 12 (2021) 2039.
- [3] S. Dong, Y. Zhao, J. Yang, X. Liu, W. Li, L. Zhang, Y. Wu, J. Sun, J. Feng, Y. Zhu, Visible-light responsive PDI/rGO composite film for the photothermal catalytic degradation of antibiotic wastewater and interfacial water evaporation, *Appl. Catal. B: Environ.* 291 (2021) 120127.
- [4] S. Li, M. Cai, Y. Liu, C. Wang, K. Lv, X. Chen, S-scheme photocatalyst TaON/ Bi_2WO_6 nanofibers with oxygen vacancies for efficient abatement of antibiotics and Cr (VI): intermediate eco-toxicity analysis and mechanistic insights, *Chin. J. Catal.* 43 (2022) 2652–2664.
- [5] Y. Guo, B. Yan, F. Deng, P. Shao, J. Zou, X. Luo, S. Zhang, X. Li, Lattice expansion boosting photocatalytic degradation performance of CuCo₂S₄ with an inherent dipole moment, *Chin. Chem. Lett.* 34 (2023) 107468.
- [6] P. Sun, Y. Zhou, H. Li, H. Zhang, L. Feng, Q. Cao, S. Liu, T. Wågberg, G. Hu, Round-the-clock bifunctional honeycomb-like nitrogen-doped carbon-decorated Co₂P/Mo₂C-heterojunction electrocatalyst for direct water splitting with 18.1% STH efficiency, *Appl. Catal. B: Environ.* 310 (2022) 121354.
- [7] H. Son, J. Lee, P. Uthirakumar, V. Dao, A. Soon, Y. Lee, I. Lee, Platinum single-atom catalysts anchored on a heterostructure cupric oxide/copper foam for accelerating photoelectrochemical hydrogen evolution reaction, *Nano Energy* 117 (2023) 108904.
- [8] K. Wang, H. Qin, J. Li, Q. Cheng, Y. Zhu, H. Hu, J. Peng, S. Chen, G. Wang, S. Chou, S. Dou, Y. Xiao, Metallic AgInS₂ nanocrystals with sulfur vacancies boost atmospheric CO₂ photoreduction under near-infrared light illumination, *Appl. Catal. B: Environ.* 332 (2023) 122763.
- [9] Z. Wang, J. Wang, J. Zhang, K. Dai, Overall utilization of photoexcited charges for simultaneous photocatalytic redox reactions, *Acta Phys. -Chim. Sin.* 39 (2023) 2209037.
- [10] X. Jin, L. Ye, H. Xie, G. Chen, Bismuth-rich bismuth oxyhalides for environmental and energy photocatalysis, *Coord. Chem. Rev.* 349 (2017) 84–101.
- [11] M. Shi, G. Li, J. Li, X. Jin, X. Tao, B. Zeng, E. Pidko, R. Li, C. Li, Intrinsic facet-dependent reactivity of well-defined BiOBr nanosheets on photocatalytic water splitting, *Angew. Chem. Int. Ed.* 59 (2020) 6590–6595.
- [12] Z. Zan, X. Li, X. Gao, J. Huang, Y. Luo, L. Han, 0D/2D carbon nitride quantum dots (CNQDs)/BiOBr S-scheme heterojunction for robust photocatalytic degradation and H₂O₂ production, *Acta Phys. -Chim. Sin.* 39 (2023) 2209016.
- [13] H. Li, J. Shang, Z. Ai, L. Zhang, Efficient visible light nitrogen fixation with BiOBr nanosheets of oxygen vacancies on the exposed {001} facets, *J. Am. Chem. Soc.* 137 (2015) 6393–6399.

[14] J. Li, R. Chen, W. Cui, X. Dong, H. Wang, K. Kim, Y. Chu, J. Sheng, Y. Sun, F. Dong, Synergistic photocatalytic decomposition of a volatile organic compound mixture: high efficiency, reaction mechanism, and long-term stability, *ACS Catal.* 10 (13) (2020) 7230–7239.

[15] P. Qiu, C. Xu, N. Zhou, H. Chen, F. Jiang, Metal-free black phosphorus nanosheets-decorated graphitic carbon nitride nanosheets with C-P bonds for excellent photocatalytic nitrogen fixation, *Appl. Catal. B: Environ.* 221 (2018) 27–35.

[16] W. Zhang, A.R. Mohamed, W.J. Ong, Z-scheme photocatalytic systems for carbon dioxide reduction: where are we now? *Angew. Chem. Int. Ed.* 59 (51) (2020) 22894–22915.

[17] W. Wang, X. Li, F. Deng, J. Liu, X. Gao, J. Huang, J. Xu, Z. Feng, Z. Chen, L. Han, Novel organic/inorganic PDI-Urea/BiOBr S-scheme heterojunction for improved photocatalytic antibiotic degradation and H₂O₂ production, *Chin. Chem. Lett.* 33 (2022) 5200–5207.

[18] Q. Chi, G. Zhu, D. Jia, W. Ye, Y. Wang, J. Wang, T. Tao, F. Xu, G. Jia, W. Li, P. Gao, Built-in electric field for photocatalytic overall water splitting through a TiO₂/BiOBr p-n heterojunction, *Nanoscale* 13 (2021) 4496–4504.

[19] S. Shen, X. Li, Y. Zhou, L. Han, Y. Xie, F. Deng, J. Huang, Z. Chen, Z. Feng, J. Xu, F. Dong, Novel BiOBr/Bi₂S₃ high-low junction prepared by molten salt method for boosting photocatalytic degradation and H₂O₂ production, *J. Mater. Sci. Technol.* 155 (2023) 148–159.

[20] P.V. Kamat, Boosting the efficiency of quantum dot sensitized solar cells through modulation of interfacial charge transfer, *Acc. Chem. Res.* 45 (11) (2012) 1906–1915.

[21] S. Dong, L. Xia, X. Chen, L. Cui, W. Zhu, Z. Lu, J. Sun, M. Fan, Interfacial and electronic band structure optimization for the adsorption and visible-light photocatalytic activity of macroscopic ZnSnO₃/graphene aerogel, *Compos. Part B: Eng.* 215 (2021) 108765.

[22] X. Li, J. Zhang, Y. Huo, K. Dai, S. Li, S. Chen, Two-dimensional sulfur- and chlorine-codoped g-C₃N₄/CdSe-amine heterostructures nanocomposite with effective interfacial charge transfer and mechanism insight, *Appl. Catal. B: Environ.* 280 (2021) 119452.

[23] Y. Hu, X. Li, W. Wang, F. Deng, L. Han, X. Gao, Z. Feng, Z. Chen, J. Huang, F. Zeng, Dong F. Bi and S co-doping g-C₃N₄ to enhance internal electric field for robust photocatalytic degradation and H₂ production, *Chin. J. Struct. Chem.* 41 (2022) 2206069–2206078.

[24] W. Zhang, M. Zhang, W. Liu, A. Yu, Molten-based defect engineering polymeric carbon nitride quantum dots with enhanced hole extraction: an efficient photoelectrochemical cell for water oxidation, *Carbon* 173 (2021) 339–349.

[25] Y. Xi, W. Chen, W. Dong, Z. Fan, K. Wang, Y. Shen, G. Tu, S. Zhong, S. Bai, Engineering an interfacial facet of S-scheme heterojunction for improved photocatalytic hydrogen evolution by modulating the internal electric field, *ACS Appl. Mater. Interfaces* 13 (33) (2021) 39491–39500.

[26] X. Zheng, L. Feng, Y. Dou, H. Guo, Y. Liang, G. Li, J. He, P. Liu, J. He, High carrier separation efficiency in morphology-controlled BiOBr/C schottky junctions for photocatalytic overall water splitting, *ACS Nano* 15 (2021) 13209–13219.

[27] X. Lv, L. Tao, M. Cao, X. Xiao, M. Wang, Y. Shen, Enhancing photoelectrochemical water oxidation efficiency via self-catalyzed oxygen evolution: a case study on TiO₂, *Nano Energy* 44 (2018) 411–418.

[28] L. Hao, H. Huang, Y. Zhang, T. Ma, Oxygen vacant semiconductor photocatalysts, *Adv. Funct. Mater.* 31 (25) (2021) 2100919.

[29] X. Li, B. Kang, F. Dong, F. Deng, L. Han, X. Gao, J. Xu, X. Hou, Z. Feng, Z. Chen, L. Liu, J. Huang, BiOBr with oxygen vacancies capture OD black phosphorus quantum dots for high efficient photocatalytic ofloxacin degradation, *Appl. Surf. Sci.* 593 (2022) 153422.

[30] X. Tong, X. Cao, T. Han, W. Cheong, R. Lin, Z. Chen, D. Wang, C. Chen, Q. Peng, Y. Li, Convenient fabrication of BiOBr ultrathin nanosheets with rich oxygen vacancies for photocatalytic selective oxidation of secondary amines, *Nano Res.* 12 (2019) 1625–1630.

[31] X. Dong, W. Zhang, Y. Sun, J. Li, W. Cen, Z. Cui, H. Huang, F. Dong, Visible-light-induced charge transfer pathway and photocatalysis mechanism on Bi semimetal@defective BiOBr hierarchical microspheres, *J. Catal.* 357 (2018) 41–50.

[32] P.M. Rao, L. Cai, C. Liu, I.S. Cho, C.H. Lee, J.M. Weisse, P. Yang, X. Zheng, Simultaneously efficient light absorption and charge separation in WO₃/BiVO₄ core/shell nanowire photoanode for photoelectrochemical water oxidation, *Nano Lett.* 14 (2014) 1099–1105.

[33] L. Xiao, W. Ren, S. Shen, M. Chen, R. Liao, Y. Zhou, X. Li, Enhancing photocatalytic hydrogen evolution through electronic structure and wettability adjustment of ZnIn₂S₄/Bi₂O₃ S-scheme heterojunction, *Acta Phys. -Chim. Sin.* 40 (8) (2024) 2308036.

[34] C. Liu, F. Meng, L. Zhang, D. Zhang, S. Wei, K. Qi, J. Fan, H. Zhang, X. Cui, CuO/ZnO heterojunction nanoarrays for enhanced photoelectrochemical water oxidation, *Appl. Surf. Sci.* 469 (2019) 276–282.

[35] R. Wang, J. Yan, M. Zu, S. Yang, X. Cai, Q. Gao, Y. Fang, S. Zhang, S. Zhang, Facile synthesis of interlocking g-C₃N₄/CdS photoanode for stable photoelectrochemical hydrogen production, *Electrochim. Acta* 279 (2018) 74–83.

[36] S. Dong, L. Cui, Y. Tian, L. Xia, Y. Wu, J. Yu, D.M. Bagley, J. Sun, M. Fan, A novel and high-performance double Z-scheme photocatalyst ZnO-SnO₂-Zn₂SnO₄ for effective removal of the biological toxicity of antibiotics, *J. Hazard. Mater.* 399 (2020) 123017.

[37] J. Zhang, L. Wang, X. Liu, X. Li, W. Huang, High-performance CdS-ZnS core-shell nanorod array photoelectrode for photoelectrochemical hydrogen generation, *J. Mater. Chem. A* 3 (2) (2015) 535–541.

[38] X. Zhang, H. Guo, G. Dong, Y. Zhang, G. Lu, Y. Bi, Homostructural Ta₃N₅ nanotube/nanoparticle photoanodes for highly efficient solar-driven water splitting, *Appl. Catal. B: Environ.* 277 (2020) 119217.

[39] M.A. Hassan, J.-H. Kang, M.A. Johar, J.-S. Ha, S.-W. Ryu, High-performance ZnS/GaN heterostructure photoanode for photoelectrochemical water splitting applications, *Acta Mater.* 146 (2018) 171–175.

[40] R. Boppella, W. Yang, J. Tan, H.-C. Kwon, J. Park, J. Moon, Black phosphorus supported Ni₂P co-catalyst on graphitic carbon nitride enabling simultaneous boosting charge separation and surface reaction, *Appl. Catal. B: Environ.* 242 (2019) 422–430.

[41] H. Yang, Y. Zhang, F. Hu, Q. Wang, Urchin-like CoP nanocrystals as hydrogen evolution reaction and oxygen reduction reaction dual-electrocatalyst with superior stability, *Nano Lett.* 15 (11) (2015) 7616–7620.

[42] X. Ma, Y. Chang, Z. Zhang, J. Tang, Forest-like NiCoP@Cu₃P supported on copper foam as a bifunctional catalyst for efficient water splitting, *J. Mater. Chem. A* 6 (5) (2018) 2100–2106.

[43] C. Lyu, C. Cao, J. Cheng, Y. Yang, K. Wu, J. Wu, W.-M. Lau, P. Qian, N. Wang, J. Zheng, Interfacial electronic structure modulation of Ni₂P/Ni₅P₄ heterostructure nanosheets for enhanced pH-universal hydrogen evolution reaction performance, *Chem. Eng. J.* 464 (2023) 142538.

[44] X. Yue, S. Yi, R. Wang, Z. Zhang, S. Qiu, A novel and highly efficient earth-abundant Cu₃P with TiO₂ "P-N" heterojunction nanophotocatalyst for hydrogen evolution from water, *Nanoscale* 8 (2016) 17516–17523.

[45] R. Shen, J. Xie, X. Lu, X. Chen, X. Li, Bifunctional Cu₃P decorated g-C₃N₄ nanosheets as a highly active and robust visible-light photocatalyst for H₂ production, *ACS Sustain. Chem. Eng.* 6 (2018) 4026–4036.

[46] S. Hua, D. Qu, L. An, W. Jiang, Y. Wen, X. Wang, Z. Sun, Highly efficient p-type Cu₃P/n-type g-C₃N₄ photocatalyst through Z-scheme charge transfer route, *Appl. Catal. B: Environ.* 240 (2019) 253–261.

[47] H. Zhou, R. Chen, C. Han, P. Wang, Z. Tong, B. Tan, Y. Huang, Z. Liu, Copper phosphide decorated g-C₃N₄ catalysts for highly efficient photocatalytic H₂ evolution, *J. Colloid Interface Sci.* 610 (2022) 126–135.

[48] J. Zhu, Y. Li, X. Wang, J. Zhao, Y. Wu, F. Li, Simultaneous phosphorylation and Bi modification of BiOBr for promoting photocatalytic CO₂ reduction, *ACS Sustain. Chem. Eng.* 7 (2019) 14953–14961.

[49] D. Liu, D. Chen, N. Li, Q. Xu, H. Li, J. He, J. Lu, Surface engineering of g-C₃N₄ by stacked BiOBr sheets rich in oxygen vacancies for boosting photocatalytic performance, *Angew. Chem. Int. Ed.* 59 (2020) 4519–4524.

[50] F. Yao, M. Jia, Q. Yang, F. Chen, Y. Zhong, S. Chen, L. He, Z. Pi, K. Hou, D. Wang, X. Li, Highly selective electrochemical nitrate reduction using copper phosphide self-supported copper foam electrode: performance, mechanism, and application, *Water Res.* 193 (2021) 116881.

[51] X. Li, J. Xiong, X. Gao, J. Ma, Z. Chen, B. Kang, J. Liu, H. Li, Z. Feng, J. Huang, Novel BP/BiOBr S-scheme nano-heterojunction for enhanced visible-light photocatalytic tetracycline removal and oxygen evolution activity, *J. Hazard. Mater.* 387 (2020) 121690.

[52] X. Li, Y. Hu, F. Dong, J. Huang, L. Han, F. Deng, Y. Luo, Y. Xie, C. He, Z. Feng, Z. Chen, Y. Zhu, Non-noble-metallic Ni₂P nanoparticles modified Ov-BiOBr with boosting photoelectrochemical hydrogen evolution without sacrificial agent, *Appl. Catal. B: Environ.* 325 (2023) 122341.

[53] X. Li, Q. Luo, L. Han, F. Deng, Y. Yang, F. Dong, Enhanced photocatalytic degradation and H₂ evolution performance of N-CDs/S-C₃N₄ S-scheme heterojunction constructed by π-π conjugate self-assembly, *J. Mater. Sci. Technol.* 114 (2022) 222–232.

[54] S.J.A. Moniz, S.A. Shevlin, X. An, Z. Guo, J. Tang, Fe₂O₃-TiO₂ nanocomposites for enhanced charge separation and photocatalytic activity, *Chem.: A Eur. J.* 20 (47) (2014) 15571–15579.

[55] P. Wang, Y. Mao, L. Li, Z. Shen, X. Luo, K. Wu, P. An, H. Wang, L. Su, Y. Li, S. Zhan, Unraveling the interfacial charge migration pathway at the atomic level in a highly efficient Z-scheme photocatalyst, *Angew. Chem. Int. Ed.* 58 (33) (2019) 11329–11334.

[56] L. Luo, Z. Gong, Y. Xu, J. Ma, H. Liu, J. Xing, J. Tang, Binary Au-Cu reaction sites decorated ZnO for selective methane oxidation to Cl oxygenates with nearly 100% selectivity at room temperature, *J. Am. Chem. Soc.* 144 (2) (2022) 740–750.

[57] M. Xie, X. Fu, L. Jing, P. Luan, Y. Feng, H. Fu, Long-Lived, Visible-Light-Excited charge carriers of TiO₂/BiVO₄ nanocomposites and their unexpected photoactivity for water splitting, *Adv. Energy Mater.* 4 (5) (2014) 1300995.

[58] H. Ren, T. Dittrich, H. Ma, J.N. Hart, S. Fengler, S. Chen, Y. Li, Y. Wang, F. Cao, M. Schieda, Y.H. Ng, Z. Xie, X. Bo, P. Koshy, L.R. Sheppard, ZhaoC, C.C. Sorrell, Manipulation of charge transport by metallic V₃O₁₆ decorated on bismuth vanadate photoelectrochemical catalyst, *Adv. Mater.* 31 (8) (2019) 1807204.

[59] X. Zhang, M. Gao, L. Qiu, J. Sheng, W. Yang, Y. Yu, Sulfur vacancies-induced "Electron Bridge" in Ni₄Mo/Sv-Zn_xCd_{1-x}S regulates electron transfer for efficient H₂-releasing photocatalysis, *J. Energy Chem.* 79 (2023) 64–71.

[60] X. Zhang, C. Zhu, L. Qiu, M. Gao, F. Tian, Y. Liu, W. Yang, Y. Yu, Concentrating photoelectrons on sulfur sites of Zn_xCd_{1-x}S to active H-OH bond of absorbed water boosts photocatalytic hydrogen generation, *Surf. Interfaces* 34 (2022) 102312.

[61] S. Shen, Z. Wang, Z. Lin, K. Song, Q. Zhang, F. Meng, L. Gu, W. Zhong, Crystalline-amorphous interfaces coupling of CoSe₂/CoP with optimized d-band center and boosted electrocatalytic hydrogen evolution, *Adv. Mater.* 34 (13) (2022) 2110631.

[62] M. Chen, R. Abazari, S. Sanati, J. Chen, M. Sun, C. Bai, A.M. Kirillov, Y. Zhou, G. Hu, Compositional engineering of HKUST-1/sulfidized NiMn-LDH on functionalized MWCNTs as remarkable bifunctional electrocatalysts for water splitting, *Carbon Energy* 5 (12) (2023) e459.